J. Fluid Mech. (2012), *vol.* 707, *pp.* 37–52.
doi:10.1017/jfm.2012.250

Experimental characterization of three-dimensional corner flows at low Reynolds numbers

J. Sznitman[1,2]†, L. Guglielmini[3], D. Clifton[1], D. Scobee[1], H. A. Stone[1] and A. J. Smits[1]

[1] Department of Mechanical and Aerospace Engineering, Princeton University, Princeton, NJ 08544, USA

[2] Department of Biomedical Engineering, Technion–Israel Institute of Technology, Haifa 32000, Israel

[3] Center for Turbulence Research, Stanford University, Stanford, CA 94305, USA

(Received 9 January 2012; revised 12 March 2012; accepted 23 May 2012;
first published online 19 July 2012)

We investigate experimentally the characteristics of the flow field that develops at low Reynolds numbers ($Re \ll 1$) around a sharp 90° corner bounded by channel walls. Two-dimensional planar velocity fields are obtained using particle image velocimetry (PIV) conducted in a towing tank filled with a silicone oil of high viscosity. We find that, in the vicinity of the corner, the steady-state flow patterns bear the signature of a three-dimensional secondary flow, characterized by counter-rotating pairs of streamwise vortical structures and identified by the presence of non-vanishing transverse velocities (u_z). These results are compared to numerical solutions of the incompressible flow as well as to predictions obtained, for a similar geometry, from an asymptotic expansion solution (Guglielmini *et al.*, *J. Fluid Mech.*, vol. 668, 2011, pp. 33–57). Furthermore, we discuss the influence of both Reynolds number and aspect ratio of the channel cross-section on the resulting secondary flows. This work represents, to the best of our knowledge, the first experimental characterization of the three-dimensional flow features arising in a pressure-driven flow near a corner at low Reynolds number.

Key words: low-Reynolds-number flows, Stokesian dynamics, general fluid mechanics

1. Introduction

In the limit of low Reynolds numbers ($Re \ll 1$), the formation of eddies and secondary flows is known to occur within bounded geometries such as cavities and ridges (Pan & Acrivos 1967; Leong & Ottino 1989; Shankar 1993; Shankar & Deshpande 2000). For geometries involving corners, low-Reynolds-number flows are well characterized for two-dimensional configurations, both analytically (Moffatt 1964; Jeffrey & Sherwood 1980) and experimentally (Taneda 1979). In the case of corner flows in bounded three-dimensional configurations, the situation is different as the flow is three-dimensional. While in recent years, a number of simulations and analytical studies have been presented on the topic (Moffatt & Mak 1998; Gomilko, Malyuga & Meleshko 2003; Yi & Bau 2003; Rusconi *et al.* 2010; Guglielmini *et al.* 2011), there is surprisingly little, if any, quantitative experimental data available. To the best

† Email address for correspondence: sznitman@bm.technion.ac.il

of our knowledge, experiments have been limited to qualitative characterizations of the boundary-driven three-dimensional flow in the neighbourhood of a corner (Hills & Moffatt 2000), or around a cylindrical object spanning the gap of a Hele-Shaw cell where the region adjacent to the object features secondary streamwise vorticity (Riegels 1938).

With the advent of microfluidic devices (e.g. 'lab-on-a-chip') operating at low *Re* (Stone, Stroock & Ajdari 2004; Squires & Quake 2005), the existence of corners and bends is a common trait of most channel configurations. For the case of pressure-driven channel flows, Lauga, Stroock & Stone (2004) demonstrated analytically that laminar low *Re* flows in microchannels must be three-dimensional if either the channel cross-section or the curvature of the centreline varies along the axial flow direction. Despite such analytical insight, velocity fields remain to be experimentally determined even for the elementary case of a generic flow around a 90° corner bounded on either side by the walls of a channel (Guglielmini *et al.* 2011). Nevertheless, some qualitative insight into the nature of such three-dimensional corner flows has emerged recently. Rusconi *et al.* (2010) demonstrated experimentally under laminar flow conditions that biofilms made of bacterial cells held together in a self-secreted polymetric matrix developed in the form of a thread, connected to the side boundary downstream of a sharp 90° corner within microfluidic channels: the biofilms were suspended exactly in the middle plane, at half the channel height. Numerical simulations uncovered the presence of streamwise counter-rotating pairs of vortical structures where the flow is three-dimensional in the vicinity of sharp or rounded corners (Guglielmini *et al.* 2011). Such findings are consistent with the locations where, according to observations, bio-filaments connect to the corner walls.

Motivated by the work of Rusconi *et al.* (2010) and the lack of experimental flow visualization available at low *Re*, we investigate here the quantitative flow field characteristics around a sharp, L-shaped corner bounded by channel walls; such geometry may be described as a reflex corner since the passage follows the bend. Our experiments are based on particle image velocimetry (PIV) measurements conducted in a towing tank, where the flow is characterized by $Re \ll 1$. The present manuscript is organized as follows. In § 2, we describe the experimental set-up and the two-dimensional velocimetry technique, as well as the computational methods and asymptotic theory. Next, in § 3 we detail quantitative properties of the base (axial) flow and the flow topology in the vicinity of the sharp corner, with an emphasis on analysing the structure of the secondary flow (i.e. orthogonal to the primary axial flow). In particular, we compare experimental data to numerical solutions of the incompressible flow field in a configuration very similar to our experimental set-up. Moreover, experimentally determined velocity profiles are compared to predictions obtained from an asymptotic expansion solution (Guglielmini *et al.* 2011) for a similar geometry, featuring an undisturbed unidirectional flow that streams around a cylinder of rectangular cross-section and spans the gap between two horizontal plane walls.

2. Experimental and numerical approaches

2.1. *Experimental apparatus*

Flow field measurements are conducted in a custom-designed towing tank (figure 1*a,b*). The tank is constructed of transparent glass with dimensions 1220 mm × 229 mm × 305 mm (length × width × height). The tank is mounted onto an aluminium base plate to which three pairs of low-friction carts (Pasco Scientific, Roseville CA) are attached and spaced equally along the length of the base plate. The pairs of carts sit

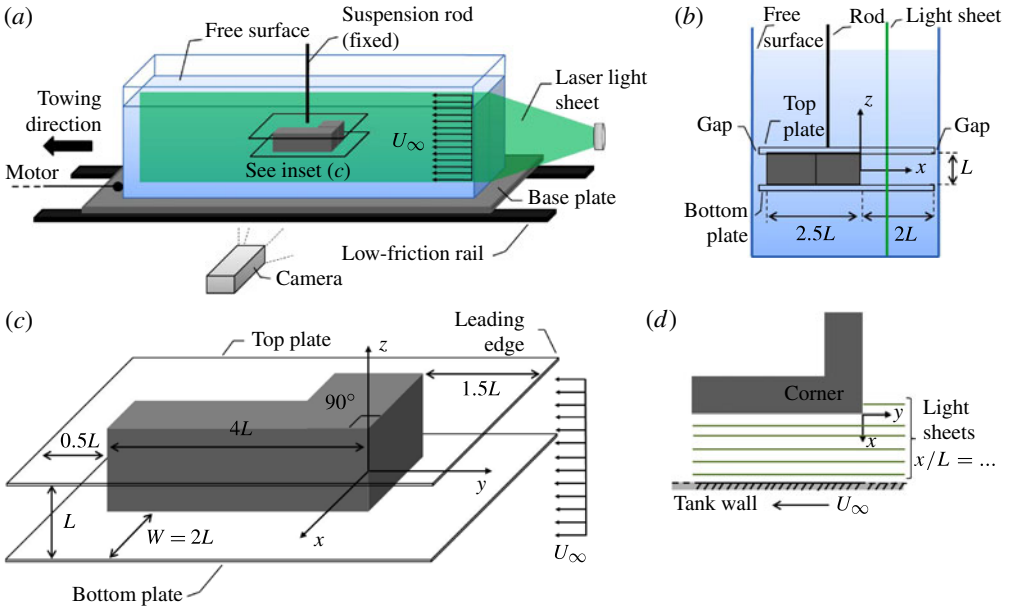

FIGURE 1. (Colour online) Schematic of the experimental apparatus. View of the towing tank along (*a*) streamwise and (*b*) spanwise directions, respectively. (*a,b*) The configuration illustrates two-dimensional planar flow field measurements in the streamwise direction (y–z plane). (*c*) Detail of the immersed obstacle constructed of an L-shaped, 90° corner sandwiched between two thin parallel plates. The height of the gap (L) between the parallel plates is chosen as the characteristic length. (*d*) Top view of the corner geometry illustrating the light sheets at fixed x/L locations (see figure 6).

on two parallel aluminium tracks (figure 1*a*) and the base plate is driven by a DC servo motor (9236 series, Pittman USA) connected to an optical encoder measuring the motor's rotational speed (r min^{-1}) and a power supply controlling the applied voltage. In the present study, only constant voltages are applied, which generate steady, linear displacements of the tank. The calibration curve of the tank speed (U_∞) versus voltage (V) is linear in the range 4–12 V ($R^2 = 0.99$), corresponding to a range of steady-state tank speeds varying from $U_\infty = 3.65 \pm 0.05$ to 12.39 ± 0.09 mm s^{-1}. Below the 4 V threshold, displacements of the tank become jerky and are thus omitted from our study. The tank is filled with a Newtonian, silicone fluid (100 % polydimethylsiloxane: Clearco Products, Bensalem PA) with viscosity $\mu_f \approx 5$ Pa s and density $\rho_f \approx 970$ kg m^{-3}.

Details of the flow geometry are shown in figure 1(*c*). The obstacle is fixed in place by a vertical rod and consists of a 'sandwich' structure made of an L-shaped, 90° corner sandwiched between two thin parallel plates (305 mm × 228 mm × 3 mm). The entire 'sandwich' is immersed in the liquid-filled tank such that the top parallel plate of the sandwich is located approximately 70 mm below the free surface (figure 1*b*). The entire structure is transparent and made of acrylic for improved optical access. Here, the height of the gap between the parallel plates is chosen as the characteristic length ($L = 50.8$ mm) and all other relevant dimensions are referenced as a function of L. The sandwich geometry is bounded by the tank wall and characterized by a channel with an aspect ratio $W/L = 2$ (i.e. width to height) downstream of the corner (figure 1*b*). Two additional configurations are also investigated where $W/L = 1$ and 3.

Note that a small gap of a few millimetres is maintained between the parallel plates and the tank wall to avoid any friction or torque on the immersed obstacle (figure 1*b*).

In our experiments, flow around the L-shaped obstacle is generated from displacing the tank in the negative y-direction with velocity U_∞, while the sandwich structure is fixed in space (figure 1*a*). The coordinate system origin lies along the edge of the corner, located halfway between the parallel plates (figure 1*c*), with the z-axis pointing upward.

2.2. *PIV measurements*

Steady flow in the vicinity of the 90° corner is investigated quantitatively using particle image velocimetry (PIV). Silver-coated hollow ceramic spheres with a diameter $d_p = 100$ μm are used as seeding particles ($\rho_p = 1.1$ g cm^{-3}: Potters Industries Inc., AG-SL150-30-TRD). Due to the high viscosity of the working fluid, the particle sedimentation rate (u_s) is slow relative to the tank speed, i.e. $U_\infty = O(1\ \text{mm s}^{-1})$, and using Stokes' law, $u_s = |\rho_f - \rho_p| d_p^2 g/(18\mu_f) \approx 0.6\ \mu\text{m s}^{-1}$, where g is the gravitational acceleration. An argon ion laser (Spectra Physic 2020) is used to create a light sheet using an optical fibre delivery system and a Powell lens (Oz Optics Ltd); the sheet thickness is typically ∼1.5 mm. Due to the slow and steady nature of the measurements, a digital SLR camera (Canon EOS 40D) is used to capture instantaneous images with a resolution of 2816×1880 pixels and a continuous acquisition rate of 5.32 frames per second. Image acquisition and the motor are triggered via computer control (Labview, National Instruments); exposure times are typically set to 1/30 s and the spatial resolution of individual images ranges between 36 and 48 μm pixel^{-1}, depending on the measurement plane investigated. Two-dimensional velocity fields are calculated between consecutive frames ($\Delta t = 0.188$ s) using an open-source, cross-correlation-based PIV code (Sveen 2004), first validated against standard PIV images (Okamoto *et al.* 2000); we find discrepancies of less than 2 % with velocity magnitudes reported in the literature.

Velocity fields are obtained both in the streamwise (y–z plane) and spanwise (x–z plane) directions by changing the camera/laser sheet configuration (figure 1*a*). Streamwise measurements are conducted by interrogating the flow at different positions in the x-direction (figure 1*b*); similarly, spanwise measurements are obtained by translating the light sheet in the y-direction. Here, steady-state velocity fields are obtained by averaging approximately 200 individual PIV images obtained at a fixed tank velocity U_∞. Note that the first few PIV images are typically omitted from the averaging scheme in an effort to exclude any possible transient effects at the onset of tank translation. We find standard deviations (SD) of the mean spatial velocity magnitude in the measurement field (e.g. y–z plane) of the order of SD ≈ 3 % or less for sequences of approximately 200 individual PIV plots upon rotating PIV data by an angle of 0.1–0.15°, due to the slight misalignment between the parallel plates of the sandwich structure and the camera's field of view. In our experiments, Re varies between 0.036 and 0.122, where $Re = \rho_f U_\infty L/\mu_f$.

2.3. *Numerical simulations and asymptotic theory*

To solve for the flow field that develops in the region confined by the two parallel plates and the sidewalls of the tank, numerical solutions of the incompressible Navier–Stokes equations are evaluated using the finite-element-based software COMSOL. Simulations employ no-slip boundary conditions at the moving and fixed walls and pressure boundary conditions at the inlet and outlet cross-sections. For each scenario simulated, the pressure drop is chosen in order for the flow rate through the channel to equal that measured in experiments (i.e. for the same thickness

of the L-shaped obstacle and the same tank velocity U_∞). The validity of the solutions discussed below is verified via successive grid refinements (i.e. the densest computational domain is made of approximately 4.5×10^5 elements). Note that sharp corners have been replaced with rounded corners of radii $R/W = 0.025$ in order to avoid geometric singularities (Guglielmini *et al.* 2011).

In addition to numerical simulations, an asymptotic expansion solution is solved for the present geometry based on the approach of Guglielmini *et al.* (2011), which follows previous studies by Thompson (1968) and Balsa (1998). In particular, we consider the flow field generated by an undisturbed unidirectional flow, which streams around a cylindrical object of rectangular cross-section (with aspect ratio 5/4, identical to that of the experimental L-shaped obstacle when mirrored with respect to the plane $x/L = -2.5$) that spans the gap between two horizontal plane walls. This configuration corresponds to the experimental geometry (figure 1) when the tank wall for negative x is replaced by a symmetry plane, in the limit $L/W \ll 1$ (i.e. the opposite tank wall is moved farther from the obstacle). As in Guglielmini *et al.* (2011), we identify an 'outer region' characterized by the typical 'potential' flow description of the 'Hele-Shaw' geometry, corresponding to a parabolic profile of the in-plane velocity along the coordinate z and a pressure distribution such that $\nabla^2_{x,y} p(x, y) = 0$, analogous to a potential flow solution. Such an 'outer' flow does not vanish at the sidewalls, but rather drives the motion in the viscous boundary layer that develops along the sidewalls. The viscous layer, or 'inner region', scales with the channel thickness L along both the vertical and the cross-stream directions and varies slowly along the streamwise direction, where we define 'streamwise' as a direction parallel to the obstacle side boundary.

In order to solve for the flow field in the 'outer region' of our specific geometry, the flow field around a cylinder is mapped into the flow field around a rectangle of aspect ratio 5/4 by a conformal transformation. The potential distribution at the cylinder surface is used to determine the pressure distribution at the rectangle surface, which provides the outer boundary condition for the viscous layer $p(\theta) = c_1 \cos\theta$, where $\theta = 0$ is the direction of the incoming flow. In Guglielmini *et al.* (2011) and in Balsa (1998), an analytical solution for the viscous boundary layer is provided and it is shown that the component of velocity u_z (i.e. the signature of the secondary flow) depends on the streamwise coordinate as the second derivative of the outer pressure field with respect to such a streamwise coordinate. Further, the vertical component of velocity u_z is antisymmetric with respect to the middle horizontal plane of the geometry and decays exponentially in the direction orthogonal to the sidewalls. In § 3, we present a comparison between the asymptotic results and the experimental and numerical results. Note that the asymptotic solution obtained for the viscous boundary layer holds only in the region along the sidewalls, approaching and leaving the corner. In the immediate proximity of the corner, the flow is anticipated to be fully three-dimensional, such that none of the spatial derivatives can be neglected and our asymptotic solution breaks down.

3. Results

3.1. *Base flow: experiments and simulations*

The steady-state velocity field in the streamwise, negative y-direction is shown in figure 2 ($Re = 0.06$). Velocity data are shown for a selection of two-dimensional y–z planes spanning the vicinity of the corner ($x_1/L = -1/4$) towards the outer tank wall ($x_7/L = 7/4$). As anticipated, the flow field arising between the top ($z/L = L/2$)

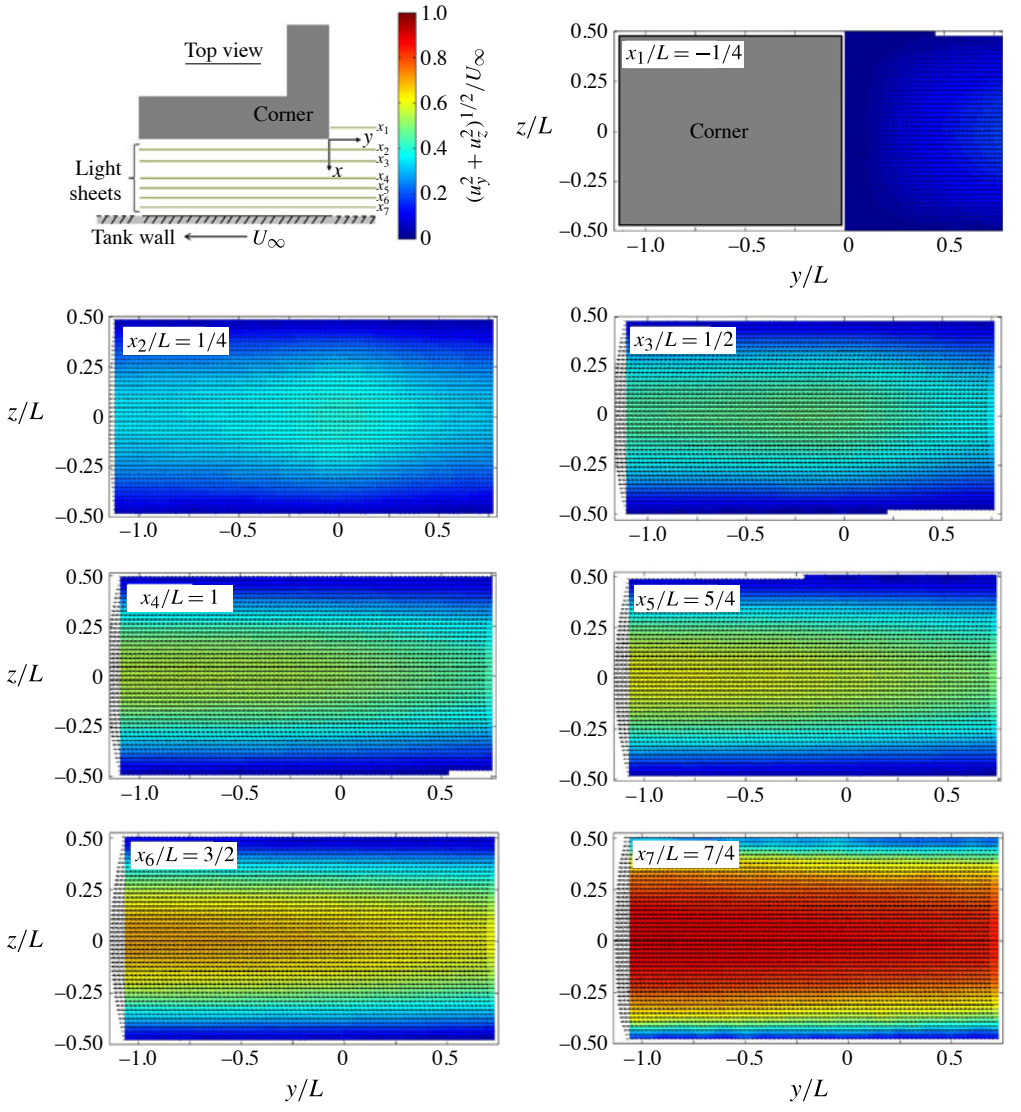

FIGURE 2. PIV measurements of the average flow field, and corresponding velocity magnitudes, obtained along the streamwise flow direction ($Re = 0.06$). A selection of PIV measurement planes are presented (x_1–x_7) and schematically depicted (a); streamwise flow is from right to left.

and bottom ($z/L = -L/2$) plates of the sandwich illustrates features of both (i) wall-bounded shear flow and (ii) fully developed laminar flow between parallel plates. On the one hand, axial flow is influenced by motion of the tank wall at $x/L = 2$ and is best understood by observing the decay in the magnitude of the flow along the negative x-direction, namely from the tank wall ($|\boldsymbol{u}(x_7)| \approx U_\infty$) towards the no-slip boundary condition at the corner ($|\boldsymbol{u}(x_2)| \to 0$). In particular, velocities along the x_1-plane are nearly quiescent (figure 2, top right-hand corner) since fluid flow must be deflected in the x-direction to get around the corner.

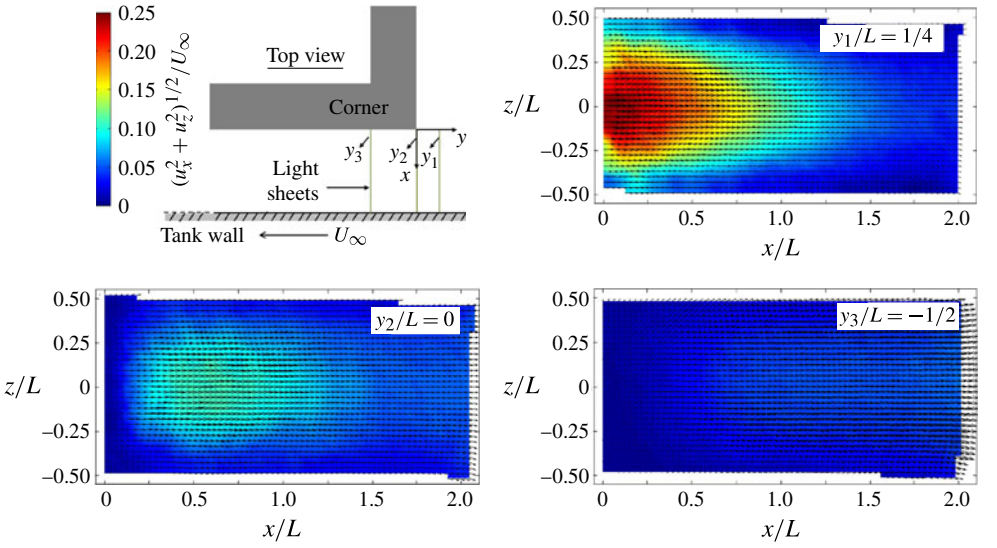

FIGURE 3. PIV measurements of the average spanwise flow field, and velocity magnitude, in the vicinity of the corner. A selection of measurement planes are shown at fixed y-positions and schematically depicted in the top left inset. Spanwise flow is from left to right.

On the other hand, due to the presence of the no-slip boundary conditions at the top and bottom plates, velocities at these locations ($z/L = L/2$ and $-L/2$, respectively) are reduced to zero (figure 2) and thus give rise to Poiseuille-like profiles, characteristic of low-Reynolds-number flows between parallel plates. It is interesting to note that in the bulk of the channel (e.g. planes x_3, x_4, and x_5), fluid flow illustrates entrance-like effects at locations proximal to the edge of the corner ($y/L > 0$). This is not surprising since fluid in the towing tank must first enter the gap created by the parallel plates but the bulk of fluid ahead of the obstacle is deflected around the stationary sandwich structure. Hence, in the rectangular ductal region away from either the corner ($x/L = 0$) or the tank wall ($x/L = 2$), flow magnitudes at the entrance of the sandwich are decelerated relative to the free-stream flow velocity U_∞ (e.g. planes x_3, x_4, and x_5, figure 2).

Further insight into the motion of fluid flow locally around the sharp corner may be gained from two-dimensional measurement planes in the spanwise x-direction. As seen in figure 3, there is a net flow ($u_x > 0$) along the y_1-measurement plane located in the region just proximal to the corner. This picture coincides with our earlier observation of nearly quiescent flow in the streamwise direction in the x_1-plane (figure 2, top right-hand corner). Note, however, that spanwise flow magnitudes in the y_1-plane remain weak ($u_x < 0.25U_\infty$) and quickly decrease as fluid approaches the tank wall ($x/L = 2$). This general trend is confirmed for measurements in the subsequent y_2- and y_3-planes (figure 3), although spanwise flow (u_x) is gradually weaker in each distal plane along the negative y-direction. Hence, sufficiently far from the corner, flow is predominantly axial and illustrates features of two-dimensional laminar channel flows (figure 2), with the exception of the presence of shear motion driven at the tank wall.

Figure 4 illustrates magnitudes of the velocity fields obtained from numerical simulations ($Re = 0.06$) in a selection of streamwise (a) and spanwise (b) planes, corresponding to experimental data shown in figures 2 and 3. In general, numerical simulations illustrate the same trends of the base flow seen in experiments, with small

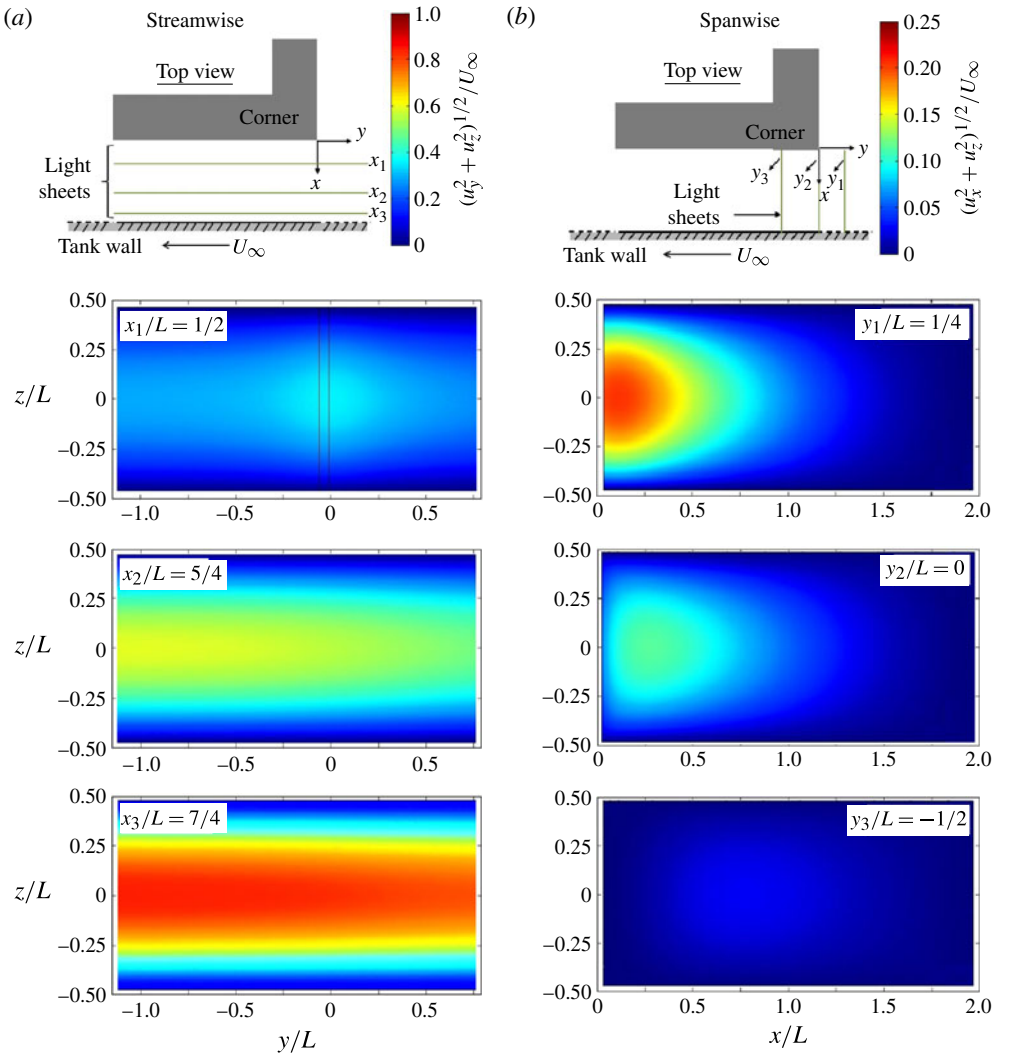

FIGURE 4. Numerical simulations of the flow field in the sandwich region of the experimental set-up shown in figure 1 ($Re = 0.06$). Results for the velocity magnitudes are shown along the streamwise (*a*) and spanwise (*b*) flow directions. A selection of streamwise planes (fixed x-position) and spanwise planes (fixed y-position) are presented. A top view of the streamwise and spanwise measurement planes is schematically depicted in the first row.

variations in the actual values of the velocity magnitudes. These trends are confirmed when investigating the resulting base flows generated for varying geometrical aspect ratios (W/L), as shown in figure 5. For the case $W/L = 2$ (figure 5*b*), numerical simulations were conducted as well for varying Reynolds number, where we generally find good agreement between experimental and numerical data. Note however that for experiments, PIV data do not cover entirely the range from $x/L = 0$ to 1.

3.2. *Secondary flow: changes with position*

We investigate features of the low-Reynolds-number flow field in the neighbourhood of the sharp corner by characterizing the secondary flow. The existence of such

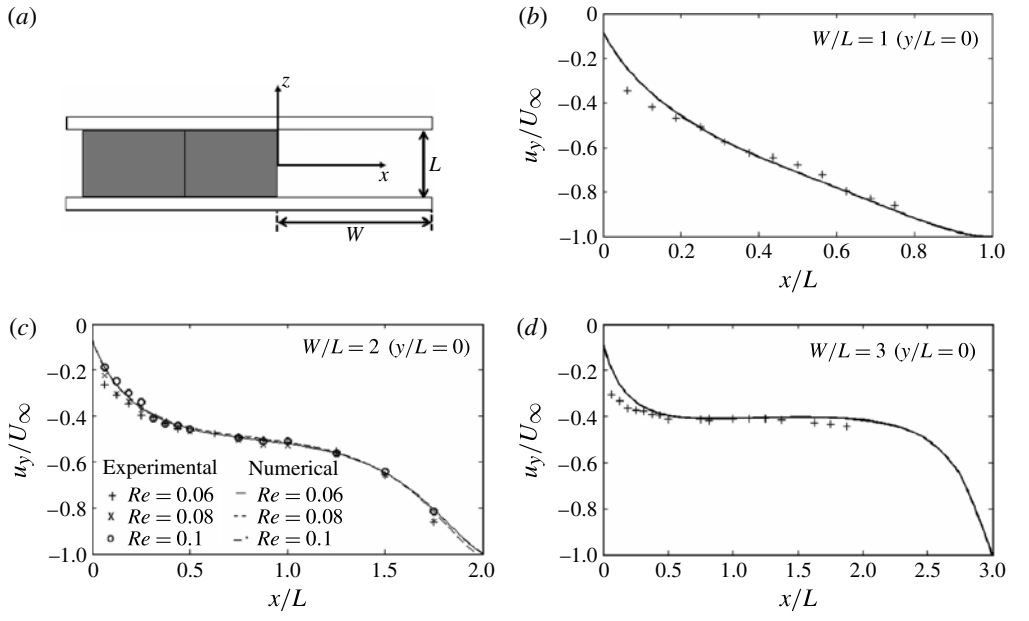

FIGURE 5. Comparisons of experimental and numerical velocity profiles of the base flow (u_y) at $Re = 0.06$ along the spanwise x-direction. A schematic of the spanwise x–z plane is shown in (a). Velocity profiles are shown for (b) $W/L = 1$, (c) $W/L = 2$, and (d) $W/L = 3$. Each velocity profile is taken at sections of constant $y = 0$ and $z = 0$, i.e. in the middle plane of the geometry. Corresponding legend for all plots of numerical (lines) and experimental (points) data is shown in plot (c).

secondary flow superimposed on the primary planar flow is best visualized in our two-dimensional measurement planes by isolating in the vicinity of the corner the u_z velocity component (figure 6). We interpret the presence of a non-vanishing u_z as the signature of a three-dimensional secondary flow (Guglielmini *et al.* 2011). Figures 6(a)–6(d) ($x/L < 0$) refer to the flow region upstream of the corner. Here, the flow streaming along the sidewall is deflected transversely to the characteristic plane of the flow (i.e. along the z-direction), in an antisymmetric fashion with respect to the middle plane of the sandwich $z = 0$ (note the upward and downward arrows in figure 6). Distal to the corner ($y/L < 0$), fluid elements experience a deflection in the opposite direction, again in an antisymmetric fashion with respect to the sandwich centreplane (figure 6e,f). Hence, the features seen before and after the turn around the sharp corner in figure 6 underlie the helical character of the secondary flow. This secondary flow consists of two pairs of counter-rotating vortices characterized by streamwise vorticity (in the direction parallel to the sidewalls), and nearly antisymmetric with respect to the middle plane of the sandwich ($z = 0$); streamwise vortices exist on length scales comparable to the height of the sandwich gap. Our experimental observations confirm the basic three-dimensional flow features seen around corners at low Re in recent numerical studies (Rusconi *et al.* 2010; Guglielmini *et al.* 2011) and identified in past analytical studies (Riegels 1938; Thompson 1968; Balsa 1998; Guglielmini *et al.* 2011).

In general, we observe that the secondary flow is characterized by slow velocities, where $|u_z|/U_\infty < 0.01$ (figure 6); that is, the strength of the transverse fluid motion

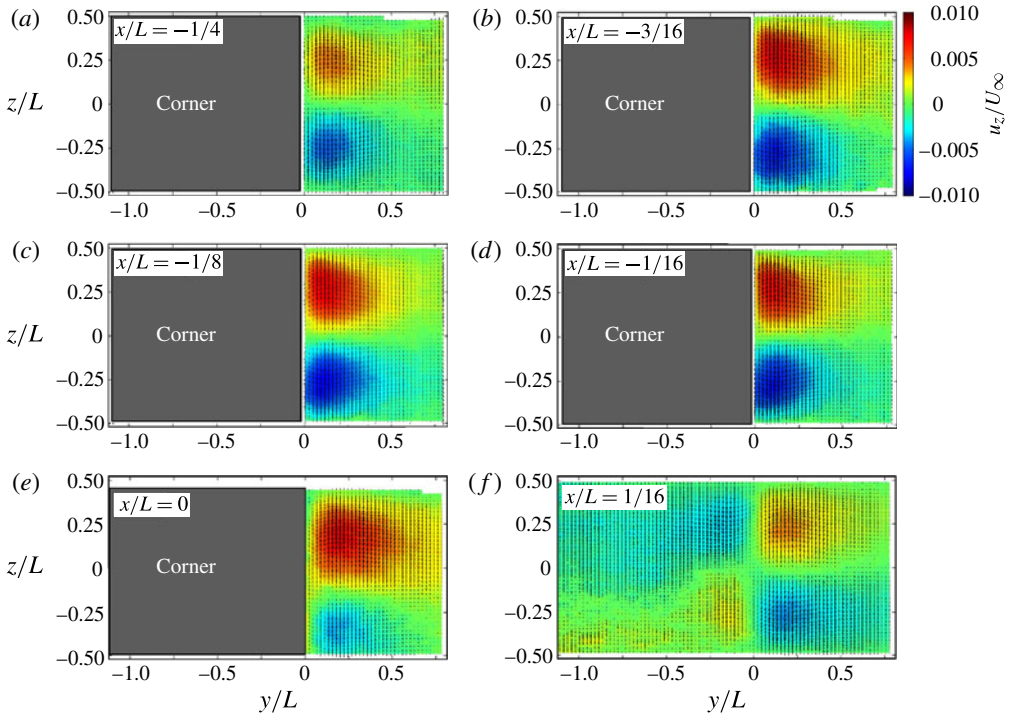

FIGURE 6. Planar PIV sections of the transverse velocity component (u_z) in the y–z plane. Measurements are shown for various sections along the x-axis ($W/L = 2$, $Re = 0.06$).

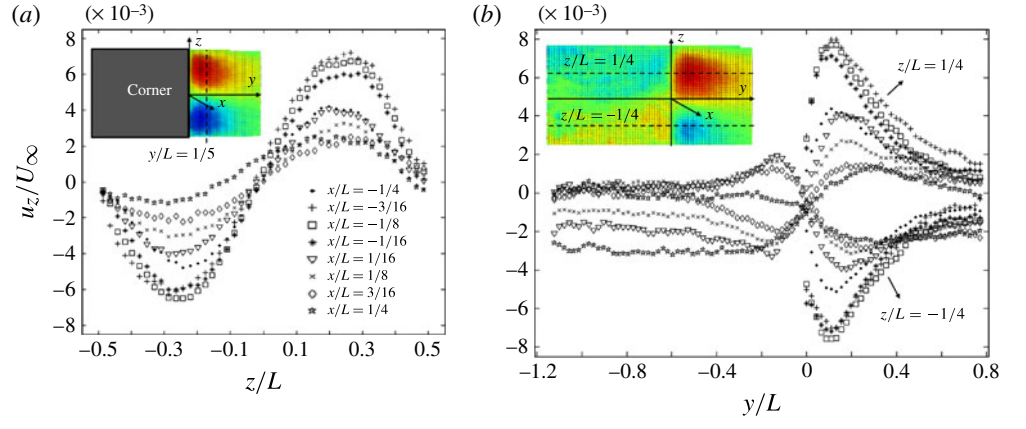

FIGURE 7. (*a*) Profiles of the transverse velocity component (u_z) along the z-axis for PIV data obtained at different x-locations ($W/L = 2$, $Re = 0.06$). Measurements are shown upstream of the corner, for a fixed $y/L = 1/5$. (*b*) Corresponding profiles of u_z along the streamwise flow direction (y-axis). PIV data are presented at two z-heights, representative of the top ($z/L = 1/4$) and bottom halves ($z/L = -1/4$) of the channel. Insets in (*a*) and (*b*) correspond to examples of two-dimensional PIV data of u_z in y–z plane for a fixed x-position ($x/L = 1/8$ and 0, respectively). Colour bar shown in figure 6.

represents merely 1 % of the velocity of the tank U_∞; note that experimental and numerical results in figure 5 indicate that the average velocity in the channel adjacent to the L-shaped obstacle is $\sim 0.5U_\infty$. Not surprisingly, these weak secondary flow structures remain entirely hidden from the primary planar flow. One-dimensional profiles of the transverse velocity component (u_z) are shown in figure 7 in an effort to characterize more precisely the evolution of these helical structures. The strength of the secondary flow upstream of the corner ($y/L > 0$) is presented in figure 7(*a*) along the axis z at the fixed position $y/L = 1/5$ and for various measurement planes at constant x. These measurements capture the nearly antisymmetric nature of the counter-rotating secondary vortices about the sandwich centreline ($z = 0$ plane). The evolution of the secondary flow strength along the axial y-direction, respectively in the top ($z/L = 1/4$) and bottom halves ($z/L = -1/4$) of the channel, is presented in figure 7(*b*) for a selection of constant x-planes. These results characterize the inversion of the secondary flow just past the sharp corner ($y = 0$). We note the clear asymmetry between the vortices before and after the turn, in which the former eddies are stronger than the latter ones. Finally, from figure 7(*b*) we can further appreciate that the magnitude of the secondary flow quickly decays distally from the corner (progressing in the negative and positive y-directions), emphasizing that the vortical phenomenon remains localized.

3.3. *Secondary flow: comparison with numerical and asymptotic theory results*

We compare PIV results for the secondary flow with numerical results. To begin with, we find that numerical contour plots of the magnitude of the transverse velocity component u_z at various planes of constant x/L (figure 8) agree well with our PIV data (figure 6). In particular, the qualitative structures of the counter-rotating secondary vortices obtained in simulations are nearly identical to those measured. Results from numerical simulations illustrate vortices of the same intensity and dependence on the spatial coordinates as those seen in the PIV visualizations. Furthermore, downstream vortices are significantly weaker than upstream vortices, confirming experimental observations. This agreement is further supported by comparing detailed one-dimensional velocity profiles obtained from numerical simulations (continuous lines) and experiments (dotted lines) in figure 9, which also reports the behaviour predicted by the described asymptotic approach (dotted lines in figure 9*b,c*).

In an effort to ease the comparison with results from asymptotic theory and provide further insight into the structure of the secondary flow, we introduce a curvilinear coordinate system (s_1, s_2, z) for the fluid region close to the corner, with the streamwise axis s_1 running along the sidewall of the obstacle in our region of interest ($s_1 = 0$ at the vertical symmetry plane of the corner) and the cross-stream axis s_2 orthogonal to the sidewall and positive in the fluid domain (see figure 9*a*). In figure 9(*b*), the vertical component of the velocity u_z is shown along the coordinate s_1/L, for values of the distance from the wall $s_2/L = \{1/8, 3/16, 1/4\}$ and two vertical positions $z/L = \pm 1/4$. Correspondingly, the vertical component of the velocity u_z is plotted along s_2/L for the positions $z/L = \pm 1/4$ and along various planes at constant $x/L = \{-3/16, -1/8, -1/16\}$ in figure 9(*c*). Finally, u_z is plotted in figure 9(*d*) versus the vertical coordinate z/L at various positions $(x/L, y/L)$ located in the upstream region of the secondary flow.

We observe that, in figure 9(*b*), for both experimental and numerical results, the dependence of u_z on s_1 shows a very similar trend to that suggested by asymptotic theory (dotted lines), which predicts that the secondary velocity will be proportional to the second derivative along the streamwise coordinate s_1 of the pressure distribution

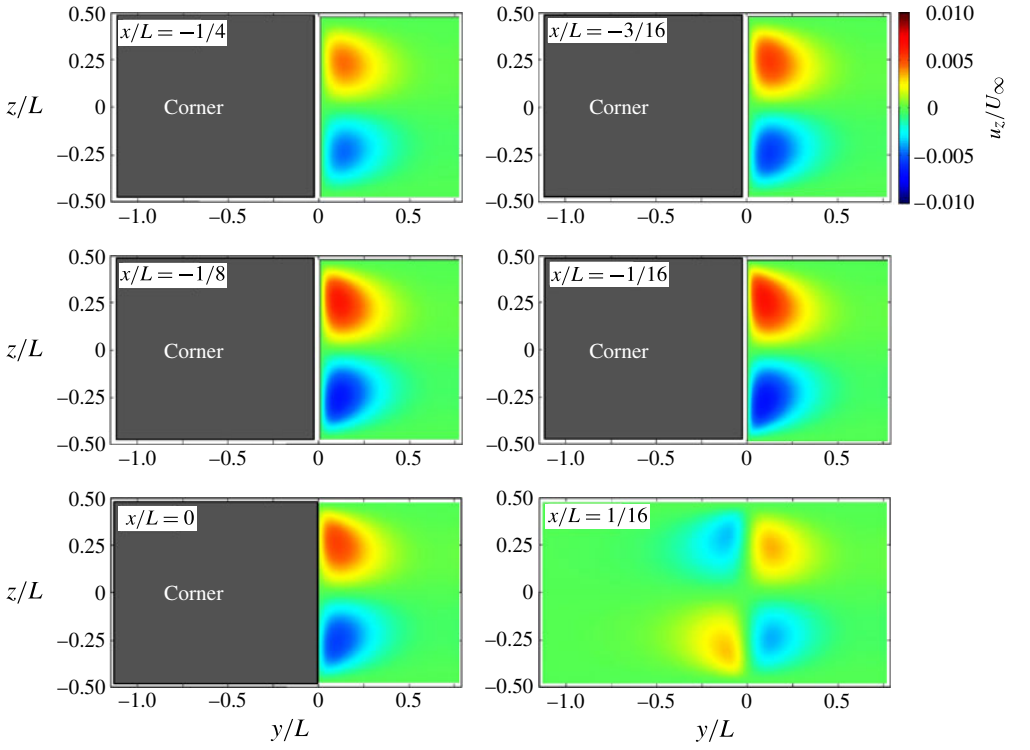

FIGURE 8. Planar PIV sections of the transverse velocity component (u_z) in the y–z plane obtained from numerical simulations ($W/L = 2$, $Re = 0.06$). Measurements are shown for identical planes presented in figure 6.

in the potential flow region ($u_z \propto \partial^2 p/\partial s_1^2$). Since we have $p(s_2 = 0) = c_1 \cos\theta$, this dependence implies a stronger secondary flow in the upstream region compared with the downstream region. In fact the second derivative of the pressure distribution in the 'outer' flow along the streamwise coordinate is larger in the upstream region ($0 < \theta < \pi/4$) than in the downstream region ($\pi/4 < \theta < \pi/2$). We believe this asymmetry to be further enhanced by features pertaining to the chosen experimental set-up, i.e. the presence of the moving tank wall at $x/L = 2$ and the non-uniformity of the in-flow into the sandwich region along the plane $y/L = 1.5$.

In addition, the velocity u_z in figure 9(c) decays exponentially moving away from the sidewall in the s_2-direction, in agreement with the solution from Balsa (1998) for the viscous boundary layer ($u_z \propto \mathrm{e}^{-2\pi s_2/L}$). Hence, we may conclude that our experiments further confirm the general structure of the secondary vorticity which develops in low-Reynolds-number flows due to variations of the curvature of the boundary, as first described by Balsa (1998) and Guglielmini *et al.* (2011).

We have systematically quantified, for figure 9 and the following figures 10 and 11, the relative error between experimental and numerical velocity distributions and found that this quantity varies between 15 and 50 %, depending on the specific experiment and region of the flow field considered. Such discrepancies are thought to arise in part from differences in the experimental and numerical profiles of the main axial flow (figure 5). This follows as the numerical geometry is slightly different from the sandwich structure used in experiments. Moreover, the inlet flow into the

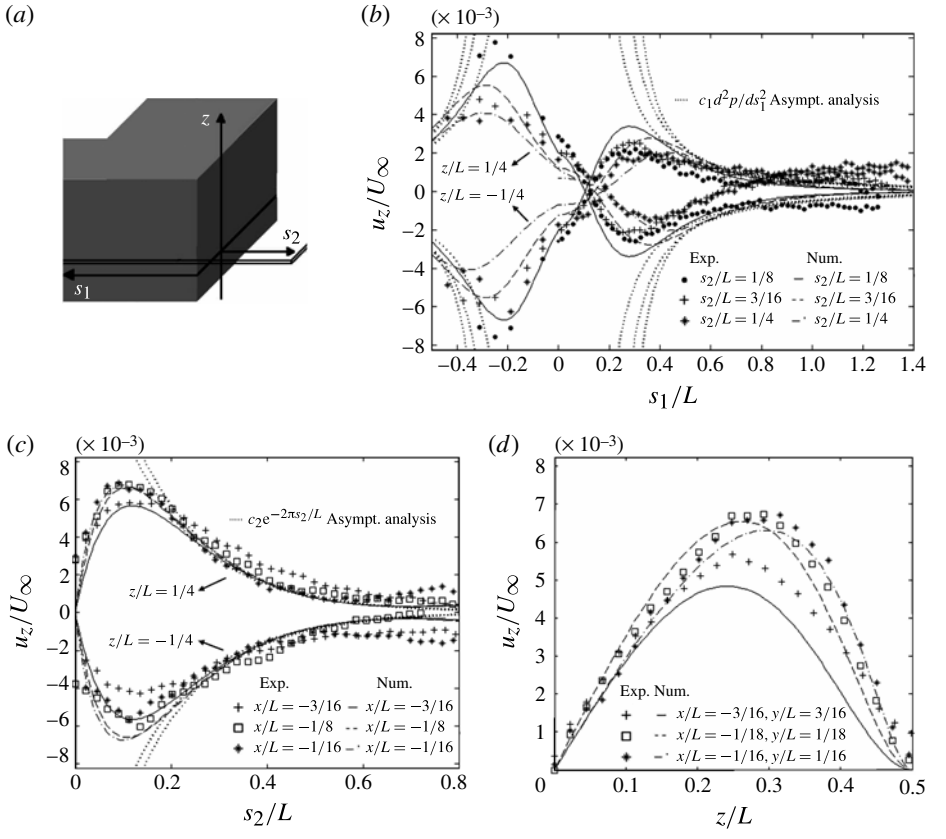

FIGURE 9. Comparison of the secondary flow ($Re = 0.06$) as obtained from experiments, numerical simulations and asymptotic analysis. (*a*) A curvilinear coordinate system (s_1, s_2, z), with s_1 running along the sidewalls and s_2 orthogonal to the sidewall. (*b*) Experimental, numerical and asymptotic results for the component of velocity u_z along the coordinate s_1 for three different values of the distance from the sidewall s_2 (see legend) and two vertical coordinates $z = \pm 1/4$. (*c*) Experimental, numerical and asymptotic results for u_z versus s_2 in three planes at constant x/L and at two vertical coordinates $z = \pm 1/4$. (*d*) Profiles of the component u_z along the coordinate z/L from experiments and numerics in the top half of the channel and at three positions $(x/L, y/L)$ located upstream of the corner.

sandwich region is taken as uniform in numerical simulations while in experiments the tank set-up generates slightly non-uniform incoming flow. Nevertheless, experimental data support all the main features of the secondary flow identified with numerical simulations.

3.4. *Secondary flow: influence of Reynolds number*

The secondary flow motion arising around the sharp corner is consistently observed at Re much smaller than unity, as illustrated by varying Re in both experiments and numerical simulations. In figure 10(*a*), we extract from figure 6 the u_z velocity profile at $Re = 0.06$ along the z-axis for $x/L = -1/16$ and $y/L = 1/16$ and compare with measurements obtained for increasing Re. Proximal to the edge of the corner (i.e. $y/L > 0$), the structure and strength of the secondary flow motion appear to be nearly identical for the range of Reynolds numbers investigated here, and lie within

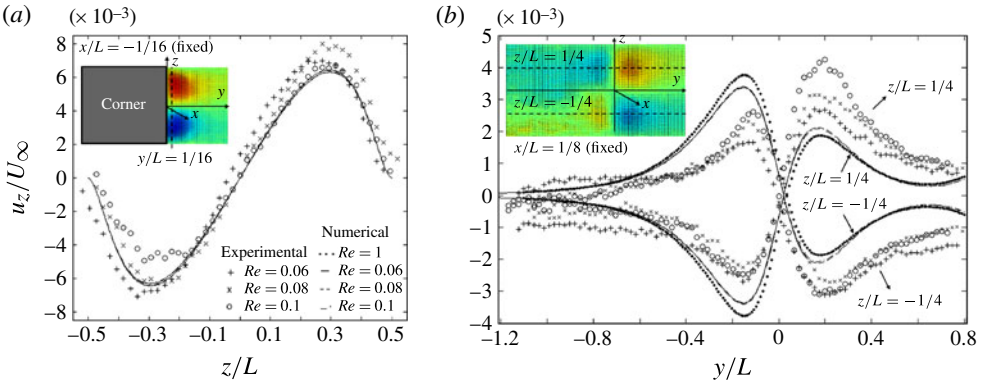

FIGURE 10. (*a*) Profiles of the transverse velocity component (u_z) along the z-axis. Measurements are shown for $W/L = 2$ and increasing values of Re, upstream of the corner for a fixed y-position ($y = L/16$). Experiments are compared with numerical simulations. (*b*) Corresponding experimental and numerical profiles of u_z along the streamwise flow direction (y-axis) for increasing Re. PIV data are shown at two z-heights, representative of the top ($z/L = 1/4$) and bottom half ($z/L = -1/4$) of the channel. Legend is given in (*a*); colour bar shown in figure 6.

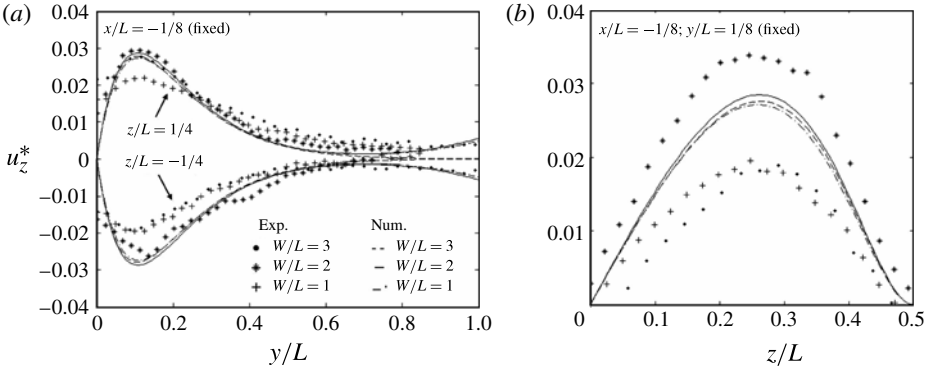

FIGURE 11. Comparison between experiments and numerical simulations of the secondary flow strength for different aspect ratios W/L ($Re = 0.06$). (*a*) Transverse velocity component (u_z^*) along the streamwise flow direction in the fixed plane $x/L = -1/8$ for data at $z/L = \pm 1/4$. (*b*) Corresponding u_z^* along the positive z-axis for fixed $x/L = -1/8$ and $y/L = 1/8$ (legend shown in *a*). In both (*a*) and (*b*), the dimensionless velocity component u_z^* is scaled with u_x at location $(-1/8, 1/8, 0)$ obtained from numerics.

the experimental error discussed above in § 3.3. Similarly, figure 10(*b*) shows velocity profiles of u_z in the streamwise y-direction for increasing Re, at z coordinates located in the top ($z/L = 1/4$) and bottom ($z/L = -1/4$) half of the channel and in the plane $x/L = 1/8$. For increasing Re, profiles again confirm the inversion of the flow direction past the sharp corner ($y = 0$) as well as the magnitude of decay of u_z distally from the corner, along the negative and positive y-direction. While velocity profiles obtained from numerical simulations are nearly identical for $Re \ll 1$, as the Reynolds number approaches unity, the upstream vortex becomes weaker while the downstream one is enhanced, in agreement with results from Guglielmini *et al.* (2011).

This latter observation allows us to conclude that the secondary flow discussed here is an inherently viscous, i.e. zero-Reynolds-number, phenomenon.

3.5. *Secondary flow: influence of channel aspect ratio W/L*

Finally, we investigate the effect on the secondary flow of the channel aspect ratio (W/L). It has been shown in Guglielmini *et al.* (2011) that for a rectangular cross-section channel performing a 90° turn, provided that the ratio of the channel height (L) and width (W) remains less than unity (conversely $W/L > 1$), the secondary flow simply rescales with L. With the aim of verifying this finding for our particular experimental set-up, we perform measurements for three different channel cross-sections ($W/L = \{1, 2, 3\}$), where we have made use of L-shaped obstacles with different widths while maintaining the same height. In figure 11, experiments and numerical simulations are reported for different ratios W/L. The secondary flows are compared by rescaling the y- and z-axis with the sandwich height (i.e. y/L and z/L), while the velocity component u_z is rescaled with the velocity parallel to the sidewall (u_x) at an arbitrary position located near the obstacle and in the middle plane. In fact, for our specific experimental apparatus, we observe that a wider channel (i.e. increase in W) leads to a smaller pressure drop through the sandwich region and, consequently, to a larger flow rate. This is accompanied by a qualitative change in the velocity profile in the channel cross-section since the flow is also driven by the boundary (see figure 5). This observation implies that the base (axial) flow cannot be rescaled in a simple way.

Following such considerations, we plot numerical and experimental results for the dimensionless velocity profile (u_z^*) along the cross-stream coordinate y for $z = \pm 1/4$ (figure 11*a*), and at a specific location in the upstream vortex (figure 11*b*). All results superimpose within the expected measurement error, at least in the region closer to the sidewall ($y/L < 0.5$). We conclude that, for a given axial flow streaming along the corner sidewalls in a shallow geometry, the structure of the secondary flow along the three coordinates rescales with the aspect ratio (W/L) of the geometry.

4. Conclusions

Until present, there are few if any available quantitative flow visualizations around a three-dimensional corner at low Reynolds numbers. We have visualized and quantified in a towing tank the secondary counter-rotating vortical structures that arise in the vicinity of such three-dimensional corners at $Re \ll 1$. Here, the specific geometry investigated consists of an L-shaped, 90° corner obstacle, sandwiched between an upper and bottom plate and sometimes referred to as a reflex corner, as the bend is followed by a passage. In particular, the top and bottom plates play a critical role in generating the three-dimensional flow. While the measured transverse flows are consistently weak in magnitude compared to the bulk streamwise flow, they remain an inherent signature of steady-state laminar creeping flows around a three-dimensional bend. In particular, our PIV data are consistent for changes in the Reynolds number, with $Re \ll 1$, as well as changes in the geometrical configuration, provided the aspect ratio W/L remains larger than unity. Experimental results have been thoroughly compared with laminar flow numerical simulations for a geometry that contains all the relevant features of the experimental set-up and with results provided by the asymptotic theory discussed in Guglielmini *et al.* (2011) and adapted for this particular flow configuration.

REFERENCES

BALSA, T. F. 1998 Secondary flow in a Hele-Shaw cell. *J. Fluid Mech.* **372**, 25–44.

GOMILKO, A. M., MALYUGA, V. S. & MELESHKO, V. V. 2003 On steady Stokes flow in a trihedral rectangular corner. *J. Fluid Mech.* **476**, 159–177.

GUGLIELMINI, L., RUSCONI, R., LECUYER, S. & STONE, H. A. 2011 Three-dimensional features in low-Reynolds-number confined corner flows. *J. Fluid Mech.* **668**, 33–57.

HILLS, C. P. & MOFFATT, H. K. 2000 Rotary honings: a variant of the Taylor paint-scraper problem. *J. Fluid Mech.* **418**, 119–135.

JEFFREY, D. J. & SHERWOOD, J. D. 1980 Streamline patterns and eddies in low-Reynolds-number flow. *J. Fluid Mech.* **96**, 315–334.

LAUGA, E., STROOCK, A. D. & STONE, H. A. 2004 Three-dimensional flows in slowly varying planar geometries. *Phys. Fluids* **16**, 3051–3062.

LEONG, C. W. & OTTINO, J. M. 1989 Experiments on mixing due to chaotic advection in the cavity. *J. Fluid Mech.* **402**, 463–469.

MOFFATT, H. K. 1964 Viscous and resistive eddies near a sharp corner. *J. Fluid Mech.* **18**, 1–18.

MOFFATT, H. K. & MAK, V. 1998 Corner singularities in three-dimensional Stokes flow. In *IUTAM Symposium on Non-linear Singularities in Deformation and Flow* (ed. D. Durban & J. R. A. Pearson), pp. 21–26. Kluwer.

OKAMOTO, K., NISHIO, S., SAGA, T. & KOBAYASHI, T. 2000 Standard images for particle-image velocimetry. *Meas. Sci. Technol.* **11**, 685–691.

PAN, F. & ACRIVOS, A. 1967 Steady flow in rectangular cavities. *J. Fluid Mech.* **28**, 643–655.

RIEGELS, F. 1938 Zur Kritik des Hele-Shaw Versuchs. *Z. Angew. Math. Mech.* **18**, 95–106.

RUSCONI, R., LECUYER, S., GUGLIELMINI, L. & STONE, H. A. 2010 Laminar flow around corners triggers the formation of biofilm streamers. *J. R. Soc. Interface* **7**, 1293–1299.

SHANKAR, P. N. 1993 The eddy structure in Stokes flow in a cavity. *J. Fluid Mech.* **250**, 371–383.

SHANKAR, P. N. & DESHPANDE, M. D. 2000 Fluid mechanics in the driven cavity. *Annu. Rev. Fluid Mech.* **32**, 93–136.

SQUIRES, T. M. & QUAKE, S. R. 2005 Microfluidics: fluid physics on the nanoliter scale. *Rev. Mod. Phys.* **77**, 977–1026.

STONE, H. A., STROOCK, A. D. & AJDARI, A. 2004 Engineering flows in small devices: microfluidics towards a lab-on-chip. *Annu. Rev. Fluid Mech.* **36**, 381–411.

SVEEN, J. K. 2004 An introduction to matPIV v. 1.6.1. *Tech. Rep.*, University of Oslo.

TANEDA, S. 1979 Visualization of separating Stokes flow. *J. Phys. Soc. Japan* **46**, 1935–1942.

THOMPSON, B. W. 1968 Secondary flow in a Hele-Shaw cell. *J. Fluid Mech.* **31**, 379–395.

YI, M. & BAU, H. H. 2003 The kinematics of bend-induced mixing in micro-conduits. *Intl J. Heat Fluid Flow* **24**, 645–656.